Validation of ADEOS-II GLI Ocean Color Products Using *In-Situ* Observations

Hiroshi Murakami[1]*, Kosei Sasaoka[2], Kohtaro Hosoda[1], Hajime Fukushima[3], Mitsuhiro Toratani[3], Robert Frouin[4], B. Greg Mitchell[4], Mati Kahru[4], Pierre-Yves Deschamps[5], Dennis Clark[6], Stephanie Flora[7], Motoaki Kishino[8], Sei-ichi Saitoh[9], Ichio Asanuma[10], Akihiko Tanaka[11], Hiroaki Sasaki[11], Katsumi Yokouchi[12], Yoko Kiyomoto[13], Hiroaki Saito[14], Cécile Dupouy[15], Absornsuda Siripong[16], Satsuki Matsumura[16] and Joji Ishizaka[17]

[1]*Earth Observation Research and Application Center, JAXA, Harumi, Chuo-ku, Tokyo 104-6023, Japan*
[2]*Frontier Research Center for Global Change, JAMSTEC, Showa-machi, Kanazawa-ku, Yokohama 236-0001, Japan*
[3]*School of High-Technology for Human Welfare, Tokai University, Numazu, Shizuoka 410-0395, Japan*
[4]*Scripps Institution of Oceanography, UCSD, La Jolla, CA 92037, U.S.A.*
[5]*Laboratoire d'Optique Atmosphérique, Université des Sciences et Technologies de Lille, Villeneuve d'Asq. Cedex, France*
[6]*National Oceanic and Atmospheric Administration, National Environmental Satellite Service, Washington, D.C., 20233, U.S.A.*
[7]*Moss Landing Marine Labs, Moss Landing, CA 95039, U.S.A.*
[8]*Marine Science, Tokyo University of Marine Science and Technology, Kohnan, Minato-ku, Tokyo 108-8477, Japan*
[9]*Fisheries Sciences and Faculty of Fisheries, Hokkaido University, Hakodate 041-8611, Japan*
[10]*Tokyo University of Information Sciences, Yato-cho, Wakaba-ku, Chiba 265-8501, Japan*
[11]*Nagasaki Industrial Promotion Foundation, Dejima-machi, Nagasaki 850-0862, Japan*
[12]*Fisheries Agency, Kasumigaseki, Chiyoda-ku, Tokyo 100-8907, Japan*
[13]*Seikai National Fisheries Research Institute, Fisheries Research Agency, Taira-machi, Nagasaki 851-2213, Japan*
[14]*Tohoku National Fisheries Research Institute, Fisheries Research Agency, Niihama, Shiogama, Miyagi 985-0001, Japan*
[15]*IRD UR103 CAMELIA, Centre d'Océanologie de Marseille, F-13007 Marseille, France*
[16]*Marine Science Department Faculty of Science, Chulalongkorn University, Bangkok 10330, Thailand*
[17]*Faculty of Fisheries, Nagasaki University, Bunkyo-machi, Nagasaki 852-8521, Japan*

The Global Imager (GLI) aboard the Advanced Earth Observing Satellite-II (ADEOS-II) made global observations from 2 April 2003 to 24 October 2003. In cooperation with several institutes and scientists, we obtained quality controlled match-ups between GLI products and *in-situ* data, 116 for chlorophyll-a concentration (CHLA), 249 for normalized water-leaving radiance (nLw) at 443 nm, and 201 for aerosol optical thickness at 865 nm (Tau_865) and Angstrom exponent between 520 and 865 nm (Angstrom). We evaluated the GLI ocean color products and investigated the causes of errors using the match-ups. The median absolute percentage differences (MedPD) between GLI and *in-situ* data were 14.1–35.7% for nLws at 380–565 nm, 52.5–74.8% nLws at 625–680 nm, 47.6% for Tau_865, 46.2% for Angstrom, and 46.6% for CHLA, values that are comparable to the ocean-color products of other sensors. We found

---

* Corresponding author. E-mail: murakami@eorc.jaxa.jp

that some errors in GLI products are correlated with observational conditions; nLw values were underestimated when nLw at 680 nm was high, CHLA was underestimated in absorptive aerosol conditions, and Tau_865 was overestimated in sunglint regions. The error correlations indicate that we need to improve the retrievals of the optical properties of absorptive aerosols and seawater and sea surface reflection for further applications, including coastal monitoring and the combined use of products from multiple sensors.

1. Introduction

The objectives of the GLI ocean science mission are to establish satellite data retrieval algorithms, to monitor physical and biological ocean variables, and to address issues of global climate change. Although it is difficult to use GLI data for monitoring purposes due to the limited data period of only seven months, we must create sufficiently accurate GLI ocean products and describe their characteristics because the GLI data will be used for algorithm development and demonstration of satellite data applications using the advantages of GLI: many (thirteen) ocean-color channels, six 250m-resolution channels, and simultaneous observation with microwave and polarization sensors, i.e., Advanced Microwave Scanning Radiometer (AMSR), POLarization and Directionality of Earth Reflectance-2 (POLDER-2), and a microwave radar sensor, SeaWinds.

Quality of satellite ocean-color products is generally assessed by comparison with simultaneous *in-situ* measurements, e.g., products of the Ocean Color Temperature Scanner (OCTS) (Shimada *et al.*, 1998; Mitomi *et al.*, 1998), POLDER instrument (Fougnie *et al.*, 1999), the Sea-viewing Wide Field-of-View Sensor (SeaWiFS) (McClain *et al.*, 2000), the Moderate-Resolution Imaging Spectrometer (MODIS) (Fargion and McClain, 2003b), and the MEdium Resolution Imaging Spectrometer (MERIS) (Bécu *et al.*, 2003). Poor quality samples are carefully excluded by referring to data flags (sunglint, observation time difference, low nLw at 555 nm, and so on) and scanning surrounding conditions (e.g., valid pixel number and variance in 3×3 pixels). In this study we investigated the accuracies of GLI products, not only under favorable condition, but also under a variety of unfavorable conditions, because the GLI operation period is limited and data users want to quantify errors and their causes in any conditions when a data pixel is not masked.

The objectives of this paper are to describe the accuracy and characteristics of the version-2 GLI ocean color products, released on 1 November 2004, in comparison to *in-situ* observations, and to clarify remaining problems for future applications and algorithm development. To address accuracies under several types of observation conditions, we investigated correlations between the errors and several variables representing observation conditions. The characteristics of GLI hardware, ocean color products, and the version-2 algorithm are given in Section 2. *In-situ* observations and their processing methods are provided in Section 3. The match-up statistics and correlation analysis are presented in Section 4. The results presented in Section 4 and reasons for the errors are discussed in Section 5.

2. GLI and Standard Ocean Color Products

2.1 GLI design

GLI is a cross-track scanning radiometer with 36 channels in the visible and near infrared (VNIR, 380 to 865 nm), shortwave infrared (SWIR, 1050 to 2210 nm), and middle and thermal infrared (MTIR, 3700 to 12000 nm) bands (Nakajima *et al.*, 1998). The GLI channels are designed not only for the ocean but also various other observation targets, including bright clouds and land surface. Tables 1 and 2 list the sensor operation and channel characteristics of GLI (Kurihara *et al.*, 2003; Tanaka *et al.*, 2005). Channels 2, 3, 6, 9, 10, 11, 12, 14, 16, and 18 are high-gain bands designed for atmospheric correction and ocean-color detection. Channels 1, 13, 15, 17, 19, 24, 25, 26, and 27 have a wide dynamic range designed for observations over land, the cryosphere, and clouds. Channels 4, 5, 7, and 8 are piece-wise linear gain bands designed for both dark and bright targets. The 250 m-resolution channels (20, 21, 22, 23, 28, and 29) were designed for compatibility with LANDSAT/TM data and other 1-km channels used for global observation. GLI also has a tilt function to prevent sun glitter, allowing accurate ocean-color observations in the summer at middle and lower latitudes.

Features of GLI sensor design compared to OCTS, SeaWiFS and MODIS are:

• Thirteen channels applicable to ocean color in visible wavelengths from 380 nm to 710 nm; OCTS and SeaWiFS have six, and MODIS ten (seven high-gain channels are used for the standard MODIS nLws).

• Twelve bit (digital numbers from 0 to 4095) digitization; OCTS and SeaWiFS are coded over ten bits (from 0 to 1023), and MODIS is the same as GLI (twelve bits).

• Tilt function (OCTS and SeaWiFS have it, but MODIS does not).

Table 1. GLI operational characteristics.

Resolution at nadir	1 km (channels 01–19, 24–27, 30–36), 250 m (20–23, 28, 29)
Field of view	Cross-track scan with 1600-km swath; observation angle ±45°; 1276 pixels (1 km L1 A) or 5104 pixels (250 m L1 A)
Detectors per scan	Along-track 12 (1 km) or 48 (250 m) detectors
Scanning mirror	Using both (A/B) sides with incident angle from 63 to 17 degrees
Digital resolution	12 bits
Orbit	Sun synchronous (descending local time about 10:30AM)
Recurrent period	4 days (57 paths)
Altitude	803 km
Period	101 min
Tilt angle	±18.5° (along track direction)
Availability	Channels 1–29, daytime (250 m, about 25% of daytime); 30–36, all times
Operation period	Dec. 2002–Oct. 2003 (global operation: Apr. 2, 2003–Oct. 24, 2003)

• Two (462 nm and 543 nm) 250-m channels in the visible range; OCTS and SeaWiFS do not have 250 m bands, and MODIS has 500 m channels in the visible range.

2.2 GLI ocean color products

GLI standard ocean color products include (a) normalized water-leaving radiance and atmospheric parameters including aerosol radiance, La (nLw and La; NL), and (b) in-water bio-optical parameters (Chlorophyll-a and Suspended matter; CS) (Table 3). NL includes nLw at 380 to 710 nm (hereafter referred to as nLw_"wavelength"), aerosol optical thickness (τ_A) at 865 nm (Tau_865), and aerosol angstrom exponent derived from τ_A at 520 nm and 865 nm (Angstrom). The GLI atmospheric correction algorithm estimates Tau_865 and Angstrom from top-of-atmosphere (TOA) radiances (L_{TOA}) at 678 nm and 865 nm, using candidate aerosol models describing optical characteristics of aerosols from "blue" (large spectral slope, generally appearing in dry and near-land areas) to "white" (low slope, generally found in humid maritime conditions). Angstrom represents the spectral slope of τ_A; high (low) values for Angstrom correspond to the blue (white) aerosols.

nLw is defined as radiance just above the sea surface with normalized atmospheric transmittance (to 1.0) and solar zenith angle (0 degrees), and is related to water reflectance (ρ_W) as follows:

$$nLw(\lambda) = \rho_W(\lambda) \times F_0(\lambda)/\pi. \quad (1)$$

Here λ is the center wavelength of GLI channels and F_0, the spectral solar irradiance at 1 AU (Thuillier *et al.*, 2003), which is weighted by the spectral responses of GLI channels (see Table 2). Photosynthetically available radiation (PAR) is defined as the number of photons per 1 m^2 over 1 day at wavelengths from 400 nm to 700 nm, and is used to estimate ocean primary productivity. CS includes major parameters that determine the seawater's optical properties: CHLA, absorption coefficient of colored dissolved organic matter at 440 nm (CDOM), suspended solid concentration (SS) defined as dry weight of filtered suspended particles except salts, and diffuse attenuation coefficient at 490 nm (K490). CHLA is used for analyses of ocean biological productivity and fishery grounds. SS and CDOM can be used as an indicator of resuspension of sediments and outflow of materials from the land.

2.3 Version 2 GLI ocean color algorithms
1) Vicarious calibration

Vicarious calibration is an indirect calibration method that assumes or models some physical processes. As such, it contrasts with a direct method, such as onboard calibration carried out using the solar diffuser or internal lamps. Ocean color algorithms require a channel-relative accuracy for L_{TOA} of better than 1%; however, the accuracy of the onboard calibrations is generally 2–3% (Xiong *et al.*, 2003; Esposito *et al.*, 2004). Vicarious calibration provides a possible way to realize such a difficult requirement.

The GLI calibration team conducted two kinds of vicarious calibration: the *in-situ* observational approach, and the global data approach. The former used nLw observed by a Marine Optical Buoy (MOBY) operated off Lanai Island in Hawaii (Clark *et al.*, 1997), along with land surface reflectance data from Railroad Valley playa (Yoshida *et al.*, 2005); whereas the latter used daily global L_{TOA} observed by GLI and L_{TOA} simulated by an atmospheric radiative transfer model based on the SeaWiFS level-3 nLw products (Murakami *et al.*, 2005). We confirmed agreement between results obtained by the *in-situ* and global approaches, and ultimately adopted the global scheme because only the global scheme can obtain many (more than 100 000/day) samples and address temporal, scan-mirror sides, and scan-angle dependencies of the

Table 2. GLI channel characteristics.

Ch	WL[d] [nm]	Width[d] [nm]	Saturation level [W/m²/str/μm]	SNR[e] (input level)	F₀[f] [W/m²/μm]
1	380.7	10	683	467 (59)	1095.7
2	399.6	9	162	1286 (70)	1540.3
3	412.3	10	130	1402 (65)	1714.6
4	442.5	9	110[a]/680	893 (54)	1885.8
5	459.3	9	124[a]/769	880 (54)	2082.0
6	489.5	11	64	1212 (43)	1939.8
7	519.2	10	92[a]/569	627 (31)	1792.5
8	544.0	10	96[a]/596	611 (28)	1858.0
9	564.8	10	39	1301 (23)	1789.0
10	624.7	10	32 (28[c])	1370 (17)	1651.2
11	666.7	10	21	1342 (13)	1522.5
12	679.9	10	22	1293 (12)	1474.7
13	678.6	10	342[c]	235 (12)	1479.0
14	710.5	11	16	1404 (10)	1394.0
15	710.1	11	233[c]	300 (10)	1396.2
16	749.0	11	11	991 (7)	1274.1
17	762.0	8	246[c]	293 (6)	1248.9
18	866.1	20	8	1309 (5)	956.0
19	865.7	10	211[c]	386 (5)	956.8

Ch	WL[d] [nm]	Width[d] [nm]	Saturation level [W/m²/str/μm]	SNR[e] (input level)	F₀[f] [W/m²/μm]
20[b]	462.4	62	691	241 (36)	1965.3
21[b]	542.1	48	585	141 (25)	1838.8
22[b]	661.3	59	107	255 (14)	1532.6
23[b]	824.1	103	235 (210[c])	218 (21)	1061.7
24	1048.6	20	227	381 (8)	654.6
25	1136.6	69	184	412 (8)	547.6
26	1241.0	18	208	303 (5.4)	454.8
27	1380.6	36	153	192 (1.5)	363.5
28[b]	1644.9	203	76	298 (5)	233.0
29[b]	2193.8	220	32	160 (1.3)	86.7

Ch	WL[d] [nm]	Width [nm]	Saturation level [Kelvin]	NEΔT [Kelvin]
30	3721.1	336	345	0.07 (at 300 K)
31	6737.5	531	307	0.03 (at 285 K)
32	7332.6	502	322	0.03 (at 300 K)
33	7511.4	526	324	0.02 (at 300 K)
34	8626.3	519	350	0.05 (at 300 K)
35	10768.0	955	354	0.05 (at 300 K)
36	12001.3	1020	358	0.06 (at 300 K)

[a] Knee points of the piece-wise linear gain channels 4, 5, 7, and 8.
[b] 250 m channels. Channels 28 and 29 are re-sampled for each 2-km (1/8) on board and stored in the 1-km product.
[c] Maximum radiance for linear response.
[d] Channel center wavelength and width derived from the GLI relative spectral responses (available in http://suzaku.eorc.jaxa.jp/GLI/cal/). GLI ocean color algorithm derives nLws at under lined thirteen channels.
[e] SNR at the standard input level (W/m²/sr/μm) was measured in pre-launch evaluation tests.
[f] Thuillier 2003 solar irradiance weighted by the GLI channel responses.

Table 3. GLI ocean color products.

Category	Variable code	Description [unit]
(a) NL	nLw_380–710	nLw at 380–710 nm (13 channels) [mW/cm^2/sr/μm]
nLw and atmospheric parameters	La_865	Aerosol radiance at 865 nm [mW/cm^2/sr/μm]
	nLw_678 and 865	Normalized water leaving radiance at 678 nm and 865 nm estimated by in-water optical model [mW/cm^2/sr/μm]
	Tau_865	Aerosol optical thickness at 865 nm
	Angstrom	Aerosol angstrom exponent between 520 nm and 865 nm
	Aalb	Aerosol albedo at 380 nm (Aalb < 1.0 means absorptive aerosol)
	PAR	Photosynthetically available radiation [Ein/m^2/day]
(b) CS	CHLA	Concentration of phytoplankton chlorophyll-a [mg/m^3]
In-water bio-optical parameters	SS	Concentration of suspended solids [g/m^3]
	CDOM	Absorption coefficients of colored dissolved organic matter at 440 nm [m^{-1}]
	K490	Diffuse attenuation coefficients at 490 nm [m^{-1}]

calibration coefficients. The calibration coefficients reduce the error of nLw_380 (root mean percentage difference from MOBY nLw_380) by about 40% (Murakami *et al.*, 2005).

2) Atmospheric correction (Fukushima, 2004)

The GLI ocean-color atmospheric correction algorithm subtracts the aerosol reflectance, which is estimated using aerosol optical thickness and spectral characteristics in near-infrared channels (678 nm and 865 nm) following Gordon (1997). This can be described by the following equations:

$$\rho_T(\lambda) = \rho_M(\lambda) + \rho_A(\lambda) + \rho_{MA}(\lambda) + T(\lambda) \times \rho_G(\lambda) + t(\lambda) \times \rho_W(\lambda) \tag{2}$$

$$\rho_T(\lambda) = [\pi L_{TOA}(\lambda)/(F_0(\lambda) \times (d_0/d)^2 \times \cos(\theta_0))]/t_{ozone}(\lambda). \tag{3}$$

Here ρ_T is top-of-atmosphere reflectance after correcting for ozone absorption, ρ_M is the reflectance due to gas molecules, ρ_A is the aerosol reflectance, ρ_{MA} is the reflectance due to the interaction between gas molecules and aerosol particles, ρ_G is the reflectance resulting from the specular reflection by direct sunlight, T is the direct transmittance of the atmosphere (from sun to surface and surface to satellite), t is the diffuse transmittance of the atmosphere (from sun to surface and surface to satellite), t_{ozone} is the transmittance of ozone, d is the distance from Earth to Sun, d_0 is 1 AU, and θ_0 is solar zenith angle.

In this process, the algorithm uses an iterative scheme to distinguish the aerosol-related reflectance ($\rho_A + \rho_{MA}$) from ρ_W, which is estimated by an in-water optical model (Tanaka *et al.*, 2004). The characteristics of the version 2 algorithm are as follows.

2.1) Absorptive aerosol correction

GLI version 2 atmospheric correction includes correction for absorptive aerosols, which appear over the oceans leeward of industrial areas or natural fires, e.g., the ocean northeast of Japan following a bush fire in Siberia occurring in summer 2003. The correction affects nLws directly in 380–520 nm when the satellite observed nLw_380 is lower than nLw_380 simulated by the in-water optical model using satellite derived CHLA, SS, and CDOM in the iterative procedure (Toratani *et al.*, 2005). It can rescue almost all negative nLws appearing in the previous version's GLI data and other satellite products. Details are described in Toratani *et al.* (2006).

2.2) Sun-glint correction

GLI version 2 atmospheric correction includes the correction of sunglint, achieved by estimating the statistical density function of the sea-surface slope by the Cox-Munk method (Cox and Munk, 1954) using wind speed data observed by SeaWinds on ADEOS-II. The correction is applied when the estimated $\rho_g \times \cos(\theta_0)/\pi$ is greater than 0.00005 and less than 0.03 (the pixel is masked when the $\rho_g \times \cos(\theta_0)/\pi$ is greater than 0.03). This enables us to derive nLw and CHLA in regions contaminated by sunglint that would otherwise be rejected and thus to increase spatial coverage.

3) Daily cloud statistics in PAR estimation (Frouin, 2004)

GLI PAR is based on the SeaWiFS PAR algorithm (Patt *et al.*, 2003), but includes a statistical daily cycle to convert the GLI observation at 10:30 local time to a daily mean. This may improve consistency with the real daily mean and enables the merging of data acquired at different local times by different sensors. Details are provided in Frouin and Murakami (2006).

4) In-water algorithm (Mitchell and Kishino, 2004)

GLI CHLA, CDOM and K490 are derived by em-

Table 4. GLI in-water algorithms and empirical equations.

Variable	Algorithm source	Algorithm type	Equation and coefficients (a_x)
CHLA	OC4-GLIv3 Modified from O'Reilly *et al.* (1998) by Mitchell and Kahru	Max Band Ratio, Modified Cubic Polynomial	CHLA $= 10^{\wedge}(a_0 + a_1 \times R + a_2 \times R^2 + a_3 \times R^3) + a_4$ $a_{0-4} = [0.531, -3.559, 4.488, -2.169, -0.230]$ $R = \log_{10}((nLw\_443 > nLw\_460 > nLw\_520)/nLw\_545)$
CDOM	Modified from Kahru and Mitchell (2001)	Linear band ratio in log-log	CDOM440 $= 10^{\wedge}(a_0 + a_1 \times R)$ $a_{0,1} = [-1.493, -1.618]$ $R = \log_{10}(nLw\_443/nLw\_520)$
K490	GLI-K490 Modified from Mitchell and Kahru (1998)	Cubic polynomial in log-log	K490 $= 10^{\wedge}(a_0 + a_1 \times R + a_2 \times R^2 + a_3 \times R^3)$ $a_{0-3} = [-0.825, -1.362, 1.094, -0.777]$ $R = \log_{10}(nLw\_460/nLw\_545)$
SS	Tanaka *et al.* (2004)	Neural network algorithm	Coefficient tables of neural networks

pirical equations using the spectral relation between nLws constructed using global *in-situ* observations (Mitchell and Kahru, 1998; Kahru and Mitchell, 1999, 2001). The empirical equations are summarized in Table 4. SS is derived with a neural-network (NN) algorithm (Tanaka *et al.*, 2004) using nLw at 412 nm, 443 nm, 460 nm, 520 nm, and 545 nm. The GLI NN algorithm is quite original and expected to improve SS in high CHLA seas (Tanaka *et al.*, 2006).

5) *Cloud detection threshold*

Cloud-detection schemes using threshold and uniformity tests have been refined to create accurate, smooth ocean color images.

(a) CLOUD_MASK is ON if $\rho_{cloud} >= 0.05$

(b) CLOUD_FLAG is ON if $\rho_{cloud} >= 0.03$

(c) near_cloud1 flag is ON if any CLOUD_MASK in around ±1 pixels

(d) near_cloud2 flag is ON if square of dispersion of $\rho_{cloud} > 0.00001$ where $\rho_{cloud} = \rho_t(ch19) - \rho_m(ch19)$.

Pixels of (a) is masked for Level-2 data, and (a), (b), and (d) are masked for Level-3 data.

3. *In-situ* Measurements and Processing

3.1 *In-situ sites and cruises*

The *in-situ* data for ocean-color validation were obtained by the GLI principal investigators, along with the National Fishery Research Institute (NFRI), Japan Coast Guard, and University of Lille, as well as volunteer investigators. We included NASA bio-Optical Marine Algorithm Data set (NOMAD) in the GLI operation period, which is compiled for bio-optical algorithm development and ocean color satellite validation activities by the NASA Ocean Biology Processing Group (Werdell and Bailey, 2005). Cruise tags, observed parameters, and *in-situ* data provider and organizations for match ups with GLI observations are listed in Table 5. Figure 1 illustrates the distribution of the match-up data. The data are distributed widely in the Pacific and Atlantic Oceans, but many data were near the coast where CHLA is generally high and the optical properties of the seawater are complex.

3.2 *In-situ data processing*

To calculate the nLw(λ), vertical profiles of the downwelling spectral irradiance Ed(λ) and the upwelling spectral radiance Lu(λ) were measured with an underwater spectroradiometer (Biospherical PRR-600, PRR-800, or MER-2040) (Ishizaka *et al.*, 2001). The underwater instruments were deployed from the sunny side of the ship to avoid any ship-shading effects. After data screening, Ed(λ) and Lu(λ) data were averaged every 1 m to remove any data spikes. Ed(λ) and Lu(λ) just below the sea surface, Ed(λ, 0⁻) and Lu(λ, 0⁻), were defined as regression coefficients fitting the data between 0 and 5–20 m (considering the pycnocline) according to the following equa-

Table 5. *In-situ* observations for GLI ocean color validation.

ID	Cruise name	nLw*	CHLA	SS	CDOM	K490	Tau	Observer/Provider
1	SIMBADA	255iv	—	—	—	—	256	Deschamps, Univ. Lille
2	SIMBAD (CalCOFI)	10v	—	—	—	—	11	Frouin, SIO
	SIMBAD (IMECOCAL)	10v	—	—	—	—	10	
	SIMBAD (P500304)	12v	—	—	—	—	12	Cutchin and Frouin, SIO
3	MOBY + AERONET	34	—	—	—	—	33	MOBY nLw by Clark, NOAA; AERONET Lanai-site by McClain and Holben
4	TriOS (Ferry 20030320)	5vi	—	—	—	—	—	Ishizaka, Nagasaki Univ. Between Nagasaki and the Goto Islands
5	TriOS (Jetfoil 20030923)	2vi	—	—	—	—	—	
	TriOS (jetfoil 20030926)	12vi	—	—	—	—	—	
6	CalCOFI (surface)	5i	41	—	1	—	—	B. G. Mitchell and Kahru, SIO
7	IMECOCAL (surface)	4ii	4	—	—	—	—	
8	Isahaya (20030414)	0i	—	—	—	—	—	
	Isahaya (20031017)	3i	2	—	—	3	—	
9	REDTIDE20030722	13i	17	15	15	13	—	
10	Nagasaki (Na03058)	0i	—	—	2	—	—	Ishizaka, Nagasaki Univ. Around the East China Sea and Ariake Bay
	Nagasaki (Na03421)	—	4	—	—	—	—	
	Nagasaki (Ka030519)	1i	2	1	2	1	—	
	Nagasaki (Na030711)	—	1	—	—	—	—	
	K030602	1i	1	1	1	1	—	
11	Kakuyo-Maru 031017	6i	8	—	—	6	—	
12	NPEC 200305	5iii	14	10	6	5	—	Ishizaka, NPEC and Nagasaki Univ.
13	Tansei-Maru 030711	—	3	—	3	—	—	Ishizaka, Nagasaki Univ.
14	Hakuho 0302	4iii	3	—	3	—	—	Sasaoka, JAXA/EORC
15	Hakodate	6iii	8	—	—	—	—	Saito, Hokkaido Univ.
16	Tokyo and Sagami-Bay	4i	11	5	5	—	—	Kishino and Ishimaru, Tokyo Kaiyo Univ.
17	New Caledonia	—	14	3	3	—	—	Dupouy and Neveux, IRD and CNRS
18	Seikai-NFRI (YK0301)	—	2	—	—	—	—	Yokouchi and Kiyomoto, Seikai NFRI YK0305is split between the East China Sea (No = 18) and NFRIAriake (19)
	Seikai-NFRI (YK0305)	1ii	5	—	—	1	—	
	Seikai-NFRI (YK0306)	0ii	0	—	—	—	—	
19	NFRIAriake (YK0305)	5ii	11	—	—	5	—	
20	Tohoku-NFRI (SPINUP)	1ii	5	—	—	1	—	Saito, Tohoku National Fisheries Research Institute Off Hokkaido and the North Pacific
	Tohoku-NFRI (SY0306)	—	3	—	—	—	—	
21	Gulf of Thai	10ii	10	10	10	10	—	Siripong and Matsumura, Chulalongkorn Univ.
22	Chiba-Monitoring Post	—	17	—	—	—	—	Japan Coast Guard
23	HCFES	—	11	—	—	—	—	Hokkaido Central Fisheries Experimental Station
24	Kurosaki	—	12	—	—	—	—	Shiomoto, National Research Institute of Fisheries Science
25	Osaka-Bay	—	1	—	—	—	—	Tarutani, National Research Institute of Fisheries and Environment of Inland Sea
26	NOMAD**	26	27	—	—	15	—	NASA Ocean Biology Processing Group (Werdell and Bailey, 2005)
—	Total	435	237	45	51	61	322	—

*Number of samples of nLw is counted as nLw_443.

**CalCOFI (0304) cruise (same as ID = 6) is excluded from the NOMAD dataset.

Instruments and observed wavelengths of nLw are follows.

i: Biospherical PRR800 λ = 380, 412, 443, 465, 490, 510, 532, 555, 565, 589, 625, 665, and 683 nm.

ii: Biospherical PRR600 λ = 412, 443, 490, 510, 555, and 565 nm.

iii: Biospherical MER2040 λ = 412, 443, 465, 490, 510, 520, 555, 565, 586, 625, 665, and 680 nm, and MER2041: 340, 380, 412, 443, 465, 490, 520, 538, 565, 585, 625, 663, and 680 nm.

iv: SIMBAD-A λ = (350, 380,) 412, 443, 490, 510, 565, 620, 670, 750, and 870 nm (above-water).

v: SIMBAD λ = 443, 490, 560, 670, and 870 nm (above-water).

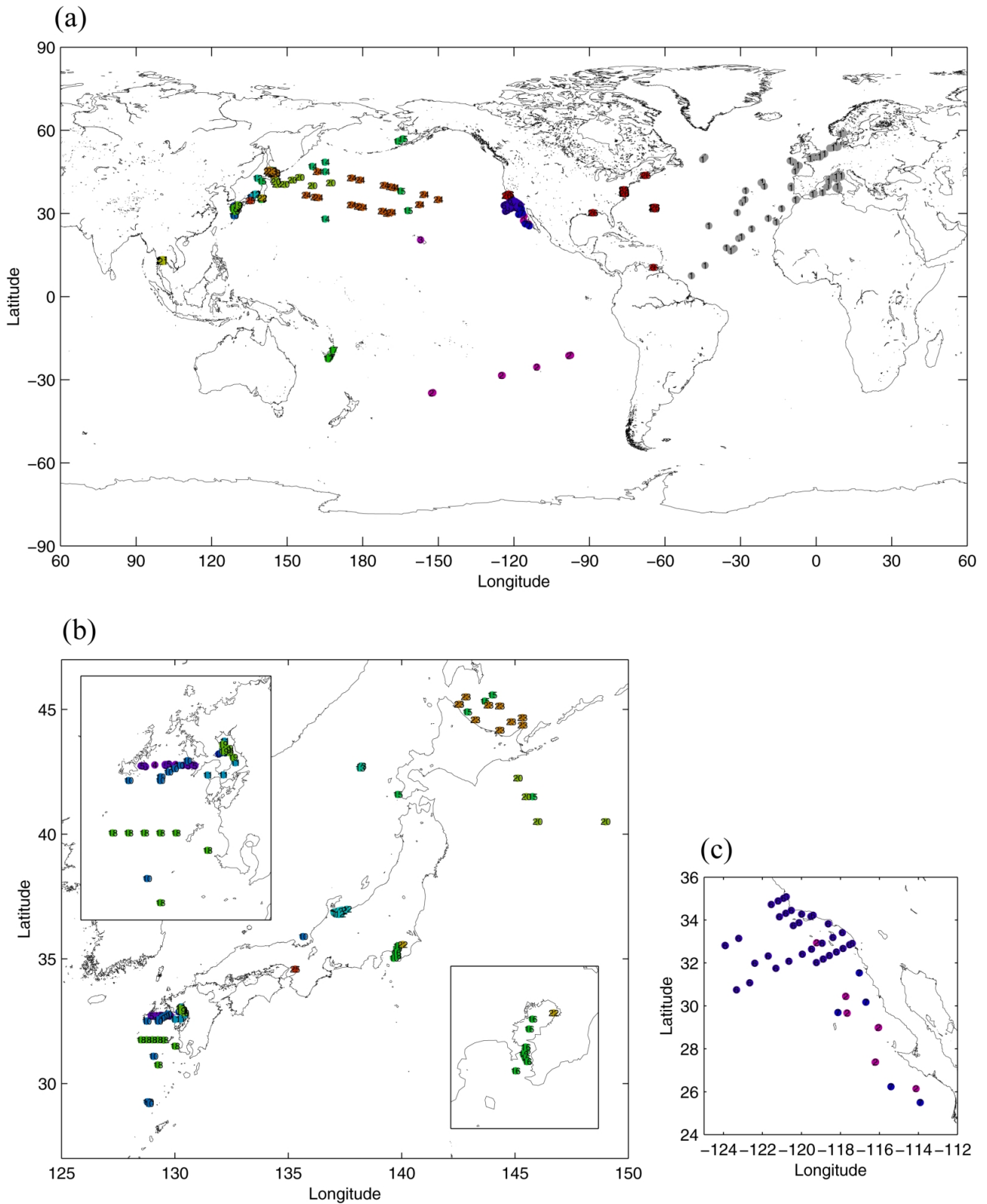vi: TriOS RAMSES multi-spectrum above-water measurements λ = 350–950 nm.

Fig. 1. Locations of the *in-situ* observations. (a) Global. (b) Around Japan. (c) Off California. Numbers in figures indicate cruises (see Table 5).

tions (Gordon and Morel, 1983):

$$Ed(\lambda, z) = Ed(\lambda, 0^-) \times e^{-Kd(\lambda) \times z}, \tag{4}$$

$$Lu(\lambda, z) = Lu(\lambda, 0^-) \times e^{-Ku(\lambda) \times z}, \tag{5}$$

where z is the depth, $Kd(\lambda)$ is the diffuse attenuation coefficient of downward irradiance, and $Ku(\lambda)$ is the diffuse attenuation coefficient of upward radiance. The water-leaving radiance, $Lw(\lambda)$, was calculated from:

$$Lw(\lambda) = t/n_w^2 \times Lu(\lambda, 0^-), \tag{6}$$

where t is the transmittance from sea to air, and n_w is the refractive index of seawater. t and n_w are approximately 0.98 and 1.341 respectively (Austin, 1974). The normalized water leaving radiance $nLw(\lambda)$ was defined as follows:

$$nLw(\lambda) = Lw(\lambda) \times F_0(\lambda)/Ed(\lambda, 0^+), \tag{7}$$

where $Ed(\lambda, 0^+)$ is incident irradiance at the sea surface calculated by on-deck instruments.

The Marine Optical Buoy (MOBY) off the Hawaiian Islands is the primary calibration site for SeaWiFS and MODIS, and has been continuously collecting $Lu(\lambda)$ at depths 1 m, 5 m, and 9 m at fine spectral resolution over the whole visible spectrum since 1996 (Clark *et al.*, 1997; Mueller *et al.*, 2003). The MOBY $Lu(\lambda)$ values were extrapolated to $Lu(\lambda, 0^-)$ and convolved with the GLI spectral response functions. Theoretically estimated $Ed(\lambda, 0^+)$ is used for the MOBY nLw in this study, as in McClain *et al.* (2000). We added Tau_865 and Angstrom data obtained by CIMEL Sunphotometer at the AErosol RObotic NETwork (AERONET) site in Lanai, Hawaii near MOBY.

Another way to obtain nLw is by making above-water optical measurements. TriOS hyperspectral radiance (RAMSES-ARC) and irradiance (RAMSES-ACC) sensors measure upwelling radiance ($Lu(\lambda, 0^+)$), downward radiance ($Ld(\lambda, 0^+)$), and $Ed(\lambda, 0^+)$. Skylight reflection on the air/sea interface have to be corrected to derive the $Lw(\lambda)$; we subtract the surface reflection assuming $Lw(\lambda = 765$ nm) to be zero.

Hand-held radiometers, called SIMBAD (Deschamps *et al.*, 2004) and SIMBADA (Bécu *et al.*, 2003) are also above-water radiometers and measure $Lu(\lambda, 0^+)$ and $Ed(\lambda, 0^+)$. $Lu(\lambda, 0^+)$ is measured with the instrument in a sea-viewing mode, while $Ed(\lambda, 0^+)$ is calculated from the τ_A measured during a sun-viewing mode measurement. The main characteristic of the instrument is the strong reduction of the reflected skylight on the air/sea interface due to polarization: the parallel component is cut by a polarizer, while the perpendicular component is cut by

viewing the sea surface near the Brewster incidence angle.

CHLA is determined by fluorometry using a spectrofluorometer for "New Caledonia" (Neveux and Lantoine, 1993; Dupouy *et al.*, 2004) and a fluorometer for other cruises after extraction by N,N-Dimethylformamide (DMF) (Suzuki and Ishimaru, 1990) or acetone. Optical densities of the CDOM in water ($ODy(\lambda)$) were measured using the multi-purpose spectrophotometer (Shimadzu MPS-2400 etc.). The spectral absorption of CDOM ($ag(\lambda)$) was calculated from measured optical density as follows:

$$ag(\lambda) = 2.303 \times ODy(\lambda)/L, \tag{8}$$

where L is the cuvette pathlength (m).

SS is derived as difference of weight of dried filter paper between before and after suction filtering and washing away sea salts on the filter, as follows:

$$SS = (W_2 - W_1)/V, \tag{9}$$

where W_1 and W_2 are filter weight before and after filtering, and V is volume of the sample water.

4. Match-up Analysis

4.1 GLI match up scheme

GLI level-1B data (L_{TOA} for each channel) were extracted within ±62 lines and pixels (about 125×125 km), and ±12 hours from the *in-situ* location and observation time (optical measurements are limited to daytime). The nearest time sample was selected if multiple observations were obtained in the same GLI 1-km pixels in the same scene. We generated GLI level-2 products for all the extracted level-1B data, and listed center pixel values, valid pixel number and standard deviation of ±1 (3×3) pixels, and cloud and land flags in ±2 (5×5) pixels for the comparison between *in-situ* and GLI parameters.

To analyze match-ups, we derived the following statistics: average of *in-situ* data (Xave), average of GLI data (Yave), ratio of GLI to *in-situ* data (Ratio), root-mean-square difference (RMSD), mean absolute percentage difference (MPD), and median absolute percentage difference (MedPD). These indexes are defined in Table 6. CHLA, SS, CDOM, and K490 were $\log_{10}$ transformed in the Xave, Yave, and RMSD calculations because they are lognormally distributed in the natural oceans (Campbell, 1995).

4.2 Results from each cruise

Figure 2 displays scatter diagrams of the match-ups for CHLA and nLw_443. Cruises are identified by index numbers (ID in Table 5), and labeled in each plot. Statis-

Table 6. Statistical equations.

	For nLw, Tau_865 and Angstrom	For CHLA, SS, CDOM and K490
Xave	$\sum_{i=1\sim N}(x_i)/N$	$10\wedge(\sum_{i=1\sim N}(\log_{10}(x_i))/N)$
Yave	$\sum_{i=1\sim N}(y_i)/N$	$10\wedge(\sum_{i=1\sim N}(\log_{10}(y_i))/N)$
RMSD	$sqrt(\sum_{i=1\sim N}((y_i-x_i)^2)/N)$	$sqrt(\sum_{i=1\sim N}((\log_{10}(y_i)-\log_{10}(x_i))^2)/N)$
Ratio		$\sum_{i=1\sim N}(y_i/x_i)/N$
MPD [%]		$\sum_{i=1\sim N}(|y_i/x_i-1|)/N\times100$
MedPD [%]		$median_{i=1\sim N}(|y_i/x_i-1|)\times100$

N: number of data samples (both *in-situ* and GLI data are valid).
x_i: *in-situ* data (i = 1~N).
y_i: GLI data (i = 1~N).
Units of Xave, Yave and RMSD for nLw and units of Xave and Yave for CHLA, SS, CDOM and K490 are mW/cm^2/sr/μm, mg/m^3, g/m^3, m^{-1}, and m^{-1} respectively.
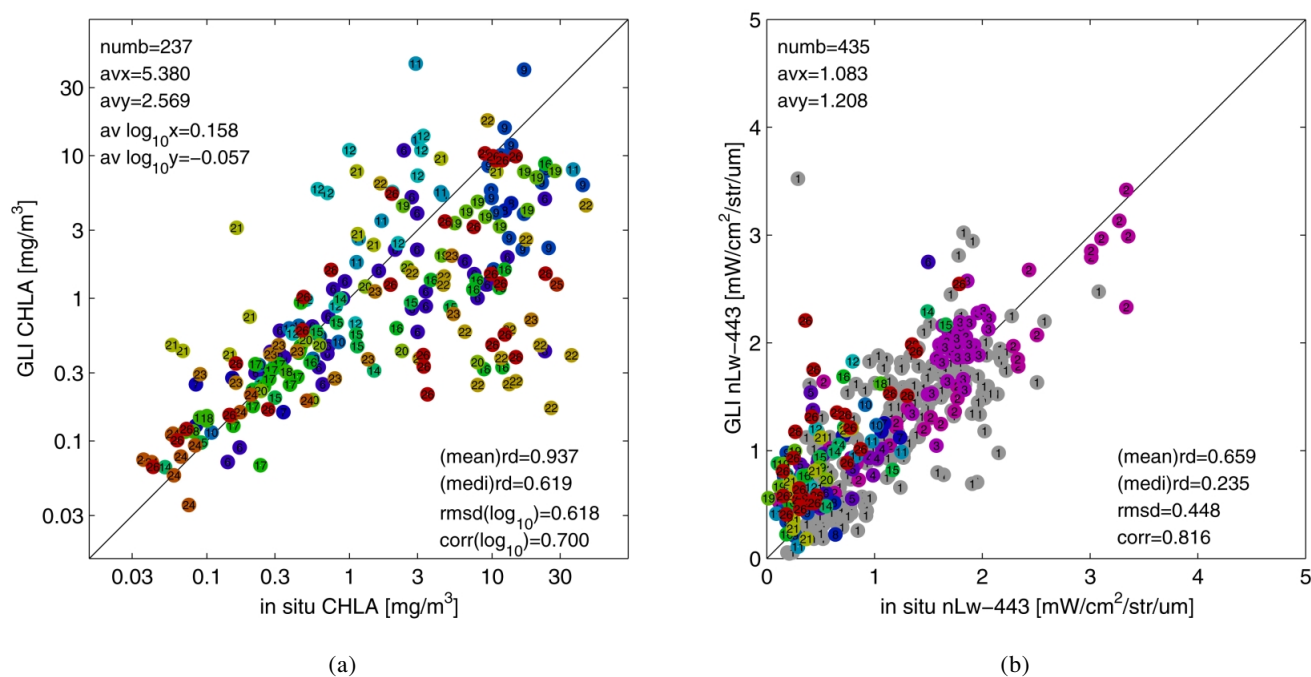

Fig. 2. Scatter diagrams of (a) CHLA and (b) nLw_443. Numbers indicate cruises.

tics for each cruise are listed in Table 7.

Large values of MPD and MedPD were observed for several cruises (e.g., gray-shaded boxes in Table 7 indicate a Ratio less than 0.5 or greater than 2.0, and MPD or MedPD greater than 100). "RedTides", "031017Ka", "Isahaya", and "NFRIAriake" are observations with high CHLA (3–15 mg/m^3) made in Ariake Bay (see Fig. 1). "TKYOSGMI" and "ChibaTHY" are observations made in Tokyo Bay that also have high CHLA (1–10 mg/m^3). "NPEC0305", "OsakaBay", and "GulfThai" are from Toyama Bay, Osaka Bay, and the Gulf of Thailand re-

spectively. These observations may have been strongly influenced by land (especially nearby large cities) and by large amounts of river runoff, and are assumed to have anomalous optical properties. In particular, the "RedTides" data measured under Red tide conditions. nLw_443 were often overestimated (Ratio >1.0) in these cruises, but CHLA were either overestimated (e.g., NPEC0305 and the GulfThai) or underestimated (e.g., cruises in Tokyo Bay). ChibaTHY and certain points of GulfThai and TKYOSGMI were obtained in shallow areas (depth less than 30 m).

Table 7. CHLA and nLw_443 match-up statistics for each cruise.

Cruises		CHLA							nLw_443						
	N	Xave	Yave	RMSD	Ratio	MPD	MedPD	N	Xave	Yave	RMSD	Ratio	MPD	MedPD
1 SIMBADA	0	—	—	—	—	—	—	255	1.155	1.190	0.442	1.14	38.6	21.5
2 SIMBAD	0	—	—	—	—	—	—	32	1.682	1.618	0.384	1.31	47.2	13.9
3 MOBY	0	—	—	—	—	—	—	34	1.761	1.934	0.289	1.10	13.5	13.2
4 FerTriOS	0	—	—	—	—	—	—	5	0.963	0.916	0.127	0.96	11.4	9.2
5 JetTriOS	0	—	—	—	—	—	—	14	0.462	0.902	0.560	2.20	125.6	103.6
6 CalCOFI	41	1.373	0.807	0.502	0.88	56.9	49.1	5	0.598	0.996	0.596	1.72	72.0	83.7
7 IMECOCAL	4	0.138	0.194	0.332	1.70	96.7	68.5	4	1.025	1.174	0.245	1.20	24.1	13.0
8 Isahaya	2	12.939	4.363	0.472	0.34	66.3	66.3	3	0.547	0.480	0.310	1.01	56.0	65.2
9 RedTides	17	14.959	6.038	0.550	0.59	60.3	67.4	13	0.236	0.548	0.400	2.61	166.3	132.7
10 Nagasaki	8	0.377	0.387	0.151	1.09	31.1	36.6	2	0.966	1.332	0.395	1.39	38.8	38.8
11 031017Ka	8	3.299	6.197	0.560	3.49	269.0	93.3	6	0.620	0.672	0.213	1.63	90.9	41.7
12 NPEC0305	14	0.995	2.377	0.536	3.55	260.1	118.2	5	0.436	1.047	0.667	2.61	160.9	130.5
13 Tansei07	3	0.240	0.236	0.021	0.98	4.7	4.4	0	—	—	—	—	—	—
14 Hakuho10	3	0.403	0.272	0.399	0.88	40.7	28.4	4	0.835	1.205	0.479	1.39	45.1	55.5
15 Hakodate	8	0.832	0.448	0.369	0.62	39.5	41.6	6	0.752	1.133	0.514	2.70	180.3	80.0
16 TKYOSGMI	11	4.553	0.855	0.862	0.31	70.7	82.8	4	0.364	0.799	0.552	2.06	105.6	128.5
17 NewCaledonia	14	0.309	0.282	0.193	1.00	26.5	13.5	0	—	—	—	—	—	—
18 Seikai-NFRI	7	0.109	0.151	0.169	1.42	46.0	46.1	1	1.058	1.622	0.563	1.53	53.2	53.2
19 NFRIAriake	11	9.434	4.402	0.406	0.56	59.9	58.6	5	0.207	0.789	0.598	10.28	927.7	473.8
20 Tohoku-NFRI	8	1.119	0.487	0.571	0.61	39.7	29.8	1	0.556	0.730	0.174	1.31	31.2	31.2
21 GulfThai	10	0.526	1.928	0.685	5.42	447.3	225.2	10	0.403	0.704	0.379	1.85	94.7	71.7
22 ChibaTHY	17	9.773	0.869	1.292	0.44	99.9	95.4	0	—	—	—	—	—	—
23 HCFESOD	11	0.934	0.521	0.588	0.97	71.4	61.9	0	—	—	—	—	—	—
24 Kurosaki	12	0.091	0.099	0.226	1.23	43.8	35.2	0	—	—	—	—	—	—
25 OsakaBay	1	28.379	1.25	1.356	0.04	95.6	95.6	0	—	—	—	—	—	—
26 NOMAD	27	2.137	0.962	0.704	0.89	67.0	68.2	26	0.608	1.115	0.648	2.33	133.4	83.0
Total	237	1.439	0.877	0.618	1.27	93.7	61.9	435	1.083	1.208	0.448	1.48	65.9	23.5

Xave, Yave, and RMSD of CHLA is converted to $\log_{10}$ before calculating the statistics.
No quality check is applied in the statistics.
Shaded boxes indicate values less than 0.5 or greater than 2.0 for Ratio, and greater than 100 for MPD and MedPD.

Table 8. CHLA and nLw_443 errors in several observation conditions.

Flags	CHLA				nLw_443				Global Area%
	N	Ratio	MPD	MedPD	N	Ratio	MPD	MedPD	
Original	237	1.27	93.7	61.9	435	1.48	65.9	23.5	100
(i) Model out of range*	38	1.61	137.0	75.9	90	1.45	66.4	48.8	32
(ii) No convergence of iteration*	8	3.11	219.7	24.1	19	1.27	63.2	30.9	1
(iii) Near cloud (cloud in 5×5)*	67	1.11	114.9	84.5	69	2.06	120.5	52.7	—
(iv) Near land (land in 5×5)*	28	1.82	177.3	93.3	19	2.34	152.2	86.2	—
(v) Thick aerosol (Tau_865 >0.25)	73	0.77	77.8	71.7	69	2.75	181.2	72.3	22
(vi) Absorptive aerosol (Aalb < 1.0)	154	1.12	94.6	66.7	229	1.61	85.0	37.1	29
(vii) low_nLw_545*	1	0.01	99.3	99.3	11	1.07	36.8	29.7	20
(viii) Sunglint $(0.03 > \rho_g \cos\theta_0/\pi > 0.00005)$	106	0.98	71.3	59.8	201	1.61	74.4	23.9	30
(ix) Shallow area (<30 m)	75	1.56	142.1	76.7	134	1.94	121.1	55.4	2
(x) Shallow than Zeu*	57	1.99	155.6	69.1	102	1.62	89.7	53.3	—
(xi) Number less than 5/9 (3×3pixels)	5	0.93	55.7	62.8	9	1.62	83.9	58.7	—
(xii) Over 20% deviation in 3×3pixels	122	1.17	98.5	69.3	83	1.61	91.8	52.7	—
(xiii) SAZ greater than 45 degrees	53	0.81	63.2	65.3	88	1.46	65.7	25.2	24
(xiv) Out of time window (3 hours)	101	1.30	87.4	44.9	105	1.42	63.8	29.3	—
(a) Exclude "*" (i)–(iv), (vii), and (x)	116	1.00	54.5	46.6	249	1.36	50.8	17.8	—
(b) Exclude (i)–(v), (vii), (ix), and (x)	81	1.08	44.9	41.2	210	1.11	26.1	16.6	—
(c) Exclude (i)–(iv), (vi)–(viii), (x)–(xii), and (xiv)	16	1.35	42.2	28.0	58	1.08	20.3	12.6	—
(d) Exclude all (i)–(xiv)	11	1.39	49.2	38.2	45	1.06	18.0	8.3	—

"Global Area" gives the percentage of pixels appearing in global equal-degree mapped data (60°N to 60°S).
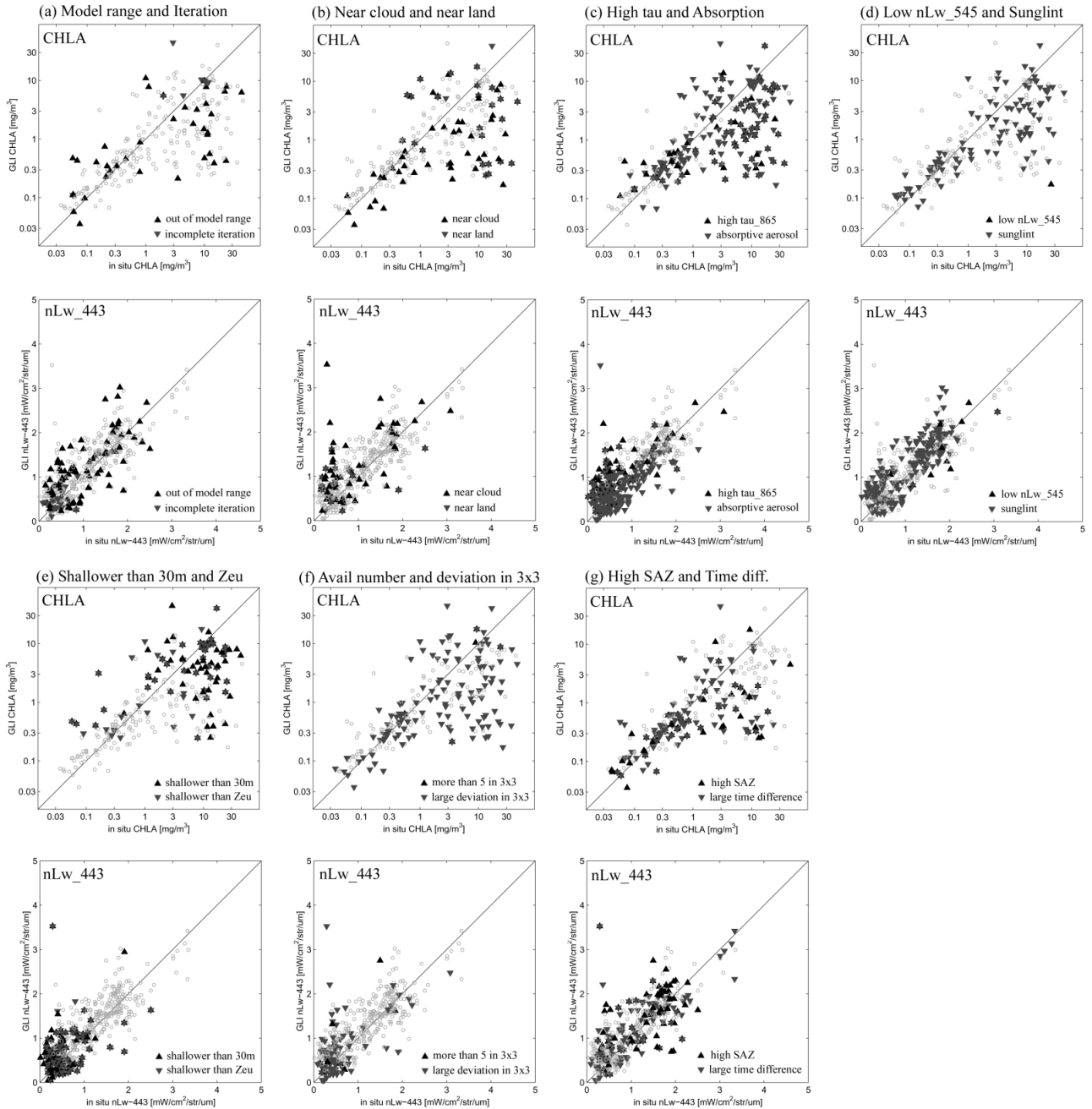Boxes of Ratio <0.5 or Ratio >2.0 or MPD >100 are shaded by gray.

Fig. 3. Flagged data for CHLA and nLw_443. Two flags are shown in every panel by upward and downward triangles.

4.3 Dependence of results on quality flags

The GLI ocean-color atmospheric correction algorithm flags for each pixel indicate that the quality of the pixel data can be degraded. We evaluated the statistics of CHLA for several level-2 flags: (i) aerosol model selection beyond the range of the prepared aerosol-model tables, (ii) no convergence of the iteration process, (vi) absorptive aerosol correction (i.e., Aalb < 1.0), (vii) low

nLw_545 (nLw_545 < 0.2), (viii) sunglint correction, and (ix) shallow water (the bottom of the sea is less than 30 m). In addition, the following situations were also evaluated: (iii) cloud neighbor (any cloud mask is on surrounding 5×5 pixels), (iv) land neighbor (any land mask is on surrounding 5×5 pixels), (v) thick aerosols (Tau_865 > 0.25), depth shallower than euphotic depth (Zeu), (xi) available pixel number less than 5 per 3×3 pixels, (xii)

variation coefficients (standard deviation/average ×100%) in 3×3 pixels more than 20%, (xiii) satellite zenith angle (SAZ) more than 45 degree, and (xiv) time difference between satellite and *in-situ* observations more than 3 hours. We calculated Zeu from *in-situ* CHLA using equations proposed by Morel and Berthon (1989). If the coincident *in-situ* CHLA was not available for nLw match ups, we calculated CHLA using the *in-situ* nLws by the equation in Table 4.

The statistics for flagged samples are listed in Table 8, and their scatter diagrams are shown in Fig. 3. MPD is extremely large (more than 100%), or Ratio is far from 1.0 (more than 2.0 or less than 0.5) in the cases (i), (ii), (iii), (iv), (vii), (ix), and (x). These flags were frequently raised in the cruise samples which showed large MPD in Table 7. For example, (vi) absorptive aerosol and (ix) shallow water flags were raised for more than half the samples of Ariake-kai cruises ("RedTides", "031017Ka", "Isahaya", and "NFRIAriake"). Almost all samples of Tokyo Bay ("TKYSGMI" and "ChibaTHY") and Osaka Bay were flagged by (iii) Near cloud and (vi) absorptive aerosol. More than half the samples of "JetTriOS" and "NPEC0305" were flagged by (iii) Near cloud, (vi) absorptive aerosol, and (viii) sunglint. Almost all samples of "GulfThai" were flagged by (ix) shallow water.

We tested a flag set (i)–(iv), (vi)–(viii), (x)–(xii), and (xiv) (labeled (c) in Table 8) similar to the SeaWiFS quality check (McClain *et al.*, 2000). SAZ range, (xiii), was not used because SAZ of GLI is always less than 60 degrees, which is the threshold of the SeaWiFS product. After the strict quality control, MPD of CHLA improved to 42.2%, but N decreased to 16, which is 6.8% of the original sample number. If all flagged samples are excluded, N decreased to 11 (Table 8(d)). Causes of the small N may be that GLI definitions and thresholds for absorptive aerosol and sunglint reflectance are different from SeaWiFS ones, and many coastal samples in the GLI match ups, in addition to the limited GLI operation period.

Percentages of the flagged samples in our match-ups are not universal (see global frequency listed in right column in Table 8) because the GLI *in-situ* observations were concentrated around coastal areas as shown in Fig. 1 and aerosol model range (i) and shallow water flags (ix) and (x) appeared more frequently in the coastal areas.

MPD of CHLA for flagged by (i)–(iv), (ix), and (x) were large (>100%) compared with the original MPD (93.7%). On the other hand, MPD was not made worse by (viii) sunglint, (xi) surrounding available pixel number, (xiii) satellite zenith angle, (xiv) and 3-hour time window. McClain *et al.* (2000) mentioned that Lw values have a dependency on solar zenith angle, and the time difference between satellite and *in-situ* observations should be less than three hours. We could not find a difference of

MPD and MedPD between samples within three hours and from three to twelve hours in the GLI match ups.

To investigate algorithm performance, we excluded samples flagged by (i), (ii), (iii), (iv), (vii), and (x) (labeled as (a) in Table 8, called QC hereafter), because they are unavoidable in the observation mechanism or irregular-processing cases when L_{TOA} might be influenced by sub-pixel land or cloud contamination, horizontal scattering from the land or cloud, and the nLw spectrum was out of range in the aerosol and in-water models. We assumed that (x) "Zeu flag" was better than (ix) "30-m depth flag" when evaluating the sea bottom effect because (ix) is raised even if the Zeu is shallower than 30 m (corresponding to CHLA > 1.63 mg/m^3). The low nLw_545 flag (vii) was used because it was often raised near cloud with an irregular nLw spectrum. MPD, MedPD and sample number of CHLA match ups were 93.7%, 61.9%, and 237 before the QC, and 54.5%, 46.6%, and 116 after the QC.

4.4 Scatter diagrams

Figure 4 and Table 9 present scatter diagrams and their statistics for nLw_380–710, Tau_865, Angstrom, CHLA, SS, CDOM, and K490 before and after the QC. Difference of sample number, N, is due to availability of *in-situ* observations. After the QC, GLI nLws agree well with the *in-situ* values at 380 to 565 nm (MPD is 23.7–82.1%, and MedPD is 14.1–35.7 after the QC). On the other hand, GLI nLw_625–680 is sometimes widely scattered from the *in-situ* data (e.g., when nLw_625–680 > 0.2 mW/cm^2/sr/μm). The reason that MPD of nLw_710 was extremely high (2139.7%) is because the values were nearly zero (from 0 to 0.03 mW/cm^2/sr/μm).

GLI Tau_865 is higher than the *in-situ* data by about double on average (Ratio = 1.98), which is due to some offset in small Tau_865 samples (averages of *in-situ* and GLI Tau_865 are 0.096 and 0.128; their difference is about 30%). Averages of *in-situ* and GLI Angstrom are 1.101 and 0.662 respectively, i.e., GLI Angstrom is smaller than the *in-situ* value on average (the opposite result, Ratio = 2.83, is due to overestimation in the near zero range).

GLI and *in-situ* CHLA agree well on average, but are sometimes scattered (underestimated) in the high-CHLA range (e.g., MPD = 80.3% and MedPD = 80.3% for *in-situ* CHLA > 3 mg/m^3). K490 is underestimated for high K490 samples (e.g., *in-situ* K490 > 0.3 m^{-1}). GLI SS was scattered in high SS range, and CDOM seems too low compared with the *in-situ* data.

4.5 Correlation among errors

We investigated correlations between parameters and errors (Table 10). Correlations with errors on Tau_865, Angstrom and nLw_565, (a), indicate characteristics of the aerosol correction; (a-1) error of aerosol spectrum represented by Angstrom, (a-2) error of aerosol amount,
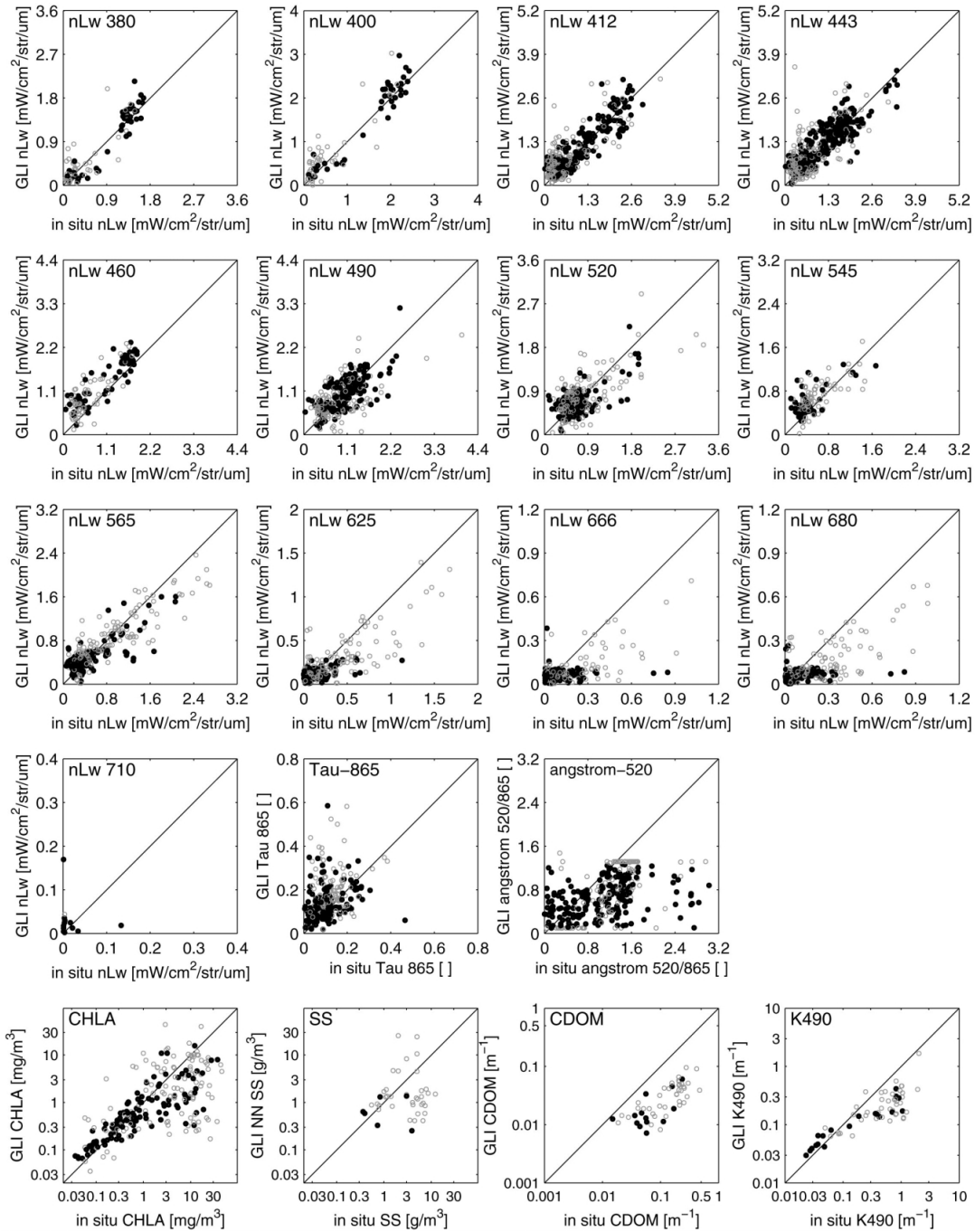
Fig. 4. Scatter diagrams of nLw_380 to 680, CHLA, SS, CDOM, K490, Tau_865, and Angstrom. Black points represent samples that passed QC; gray circle, samples screened by QC.

Tau_865, and (a-3) nLw errors at several wavelengths. Correlations between *in-situ* nLw_680 and other parameters, (b), indicate errors in highly turbid (i.e., Case-2) waters where the errors may be caused by estimation error of nLws at NIR channels by in-water model in the iteration procedure. Correlations between Aalb and oth-

ers, (c), show errors related to absorptive aerosol and GLI absorptive aerosol correction. Correlations between sunglint reflectance and others, (d), show errors related to sunglint and the GLI sunglint correction.

Errors of nLws are correlated negatively with Angstrom (Table 10(a-1)), because overestimation (un-

Table 9. Match-up statistics of GLI ocean-color products.

Name	Original							After QC						
	N	Xave	Yave	RMSD	Ratio	MPD	MedPD	N	Xave	Yave	RMSD	Ratio	MPD	MedPD
nLw_380	85	0.713	0.748	0.258	1.33	60.8	28.2	42	1.009	1.014	0.223	1.03	31.0	16.3
nLw_400	83	1.059	1.157	0.321	1.35	53.3	22.4	41	1.500	1.552	0.259	1.09	23.7	14.1
nLw_412	328	0.938	1.058	0.413	1.63	80.9	29.2	173	1.200	1.253	0.345	1.44	61.4	19.0
nLw_443	435	1.083	1.208	0.448	1.48	65.9	23.5	249	1.270	1.348	0.356	1.36	50.8	17.8
nLw_460	124	0.864	1.176	0.426	1.81	87.0	43.2	57	1.105	1.406	0.408	1.78	82.1	24.0
nLw_490	367	1.016	1.022	0.358	1.15	36.9	18.8	221	1.092	1.110	0.299	1.16	33.3	16.1
nLw_520	385	0.706	0.716	0.353	1.17	39.5	25.0	211	0.650	0.651	0.232	1.15	35.1	19.4
nLw_545	126	0.505	0.630	0.259	1.47	58.2	36.0	57	0.419	0.560	0.252	1.60	66.1	35.7
nLw_565	343	0.595	0.596	0.265	1.29	48.3	28.8	202	0.421	0.451	0.212	1.38	52.7	30.0
nLw_625	335	0.218	0.179	0.203	3.27	265.5	60.2	193	0.106	0.113	0.120	4.28	353.7	74.8
nLw_666	265	0.131	0.079	0.161	1.98	152.9	62.5	185	0.077	0.056	0.108	2.29	173.0	62.5
nLw_680	307	0.146	0.089	0.160	1.84	142.4	53.1	200	0.077	0.052	0.102	2.11	160.4	52.5
nLw_710	13	0.017	0.031	0.060	21.36	2073.0	757.1	12	0.018	0.030	0.061	22.00	2139.7	616.1
Tau_865	322	0.104	0.149	0.103	2.06	120.9	53.6	201	0.095	0.125	0.086	2.01	117.8	47.6
Angstrom	322	1.143	0.719	0.730	2.17	188.2	43.5	201	1.066	0.639	0.768	3.03	273.2	46.2
CHLA	237	1.439	0.877	0.618	1.27	93.7	61.9	116	0.796	0.563	0.448	1.00	54.5	46.6
SS	41	2.587	1.361	0.632	1.22	106.6	77.3	6	0.997	0.616	0.544	0.97	64.6	56.2
CDOM	51	0.110	0.025	0.685	0.27	73.2	78.2	13	0.064	0.016	0.650	0.31	69.5	74.3
K490	61	0.323	0.160	0.433	0.63	51.9	57.0	19	0.142	0.097	0.347	0.85	46.8	43.4

Xave, Yave, and RMSD of CHLA, SS, CDOM and K490 were Log_{10} transformed before the statistic calculations.
Boxes of Ratio <0.5 or Ratio >2.0 or MPD >100 are shaded by gray.

Table 10. Correlations between errors and variables.

Variable	Correlation coefficient between variables and (GLI-in situ)					
	Angstrom	Tau_865	nLw_443	nLw_565	nLw_680	CHLA
(a-1) Aerosol spectrum: Angstrom error (GLI-in situ)	—	−0.31	−0.31	−0.20	−0.22	no data
(a-2) Aerosol optical thickness: Tau_865error	—	—	0.20	0.07	0.08	no data
(a-3) nLw errors: nLw_565error	—	—	0.69	—	0.70	−0.32
(b) High nLw_680: in-situ nLw_680	0.19	−0.04	−0.41	−0.70	−0.95	0.14
(c) Absorptive aerosol: Aalb (a small Aalb means strong absorption)	−0.16	−0.06	0.02	0.25	0.29	0.24
(d) Sunglint: sunglint reflectance	0.10	0.26	0.35	0.21	0.11	−0.01

Underlines and gray boxes mean that the correlations (r) are more than 95% significant (t > 95% significance level of t-distribution for N, where t = sqrt(N − 2)×corr/sqrt(1 − r²)).
CHLA is converted by $\log_{10}$ scale before calculating the correlations.

derestimation) of the Angstrom (i.e., spectral slope of aerosol reflectance) causes overestimation (underestimation) of $\rho_A + \rho_{MA}$ at visible channels and that in turn causes underestimation (overestimation) of nLw at visible channels (see Figs. 5(5) and (6)). Negative correlation between Angstrom and Tau_865 indicates that errors of Tau_865 and Angstrom act in opposite directions for nLw errors; underestimation of angstrom makes nLw high but simultaneous overestimation of Tau_865 makes nLw low. We found a positive correlation between Tau_865 and nLw_443 that seems to be an opposite relation to that supposed in Eq. (2), and strong correlations between errors in nLws (a-3). The reasons for the correlation are discussed in Section 5.

When *in-situ* nLw_680 was very high (e.g., more than 0.3 mW/cm²/sr/μm), nLw values were underestimated. In contrast, there was no significant correlation between the nLw_680 error and the CHLA error.

When the absorption was strong (Aalb << 1.0), nLw in green to red channels and CHLA were underestimated (see, Figs. 5(8)–(9)–(6)–(7)). When sunglint was excessive, Tau_865 and nLw_443 were estimated too high (see, Figs. 5(2)–(3)). In contrast, there were no significant correlations between sunglint and errors of Angstrom, nLw_680, and CHLA. The correlations are discussed and interpreted in Subsection 5.3.

5. Summary and Conclusions

5.1 GLI ocean color product accuracy

We obtained 237 GLI and *in-situ* match-ups for CHLA (116 after the QC) and 435 match-ups for nLw_443 (249 after the QC). The match-up data after the QC shows that MedPD were 14.1 to 35.7% for nLws at 380 to 565 nm, 52.5 to 74.8% for nLws at 625 to 680 nm, 47.6% for Tau_865, 46.2% for Angstrom, 46.6% for CHLA, 56.2% for SS, 74.3% for CDOM, and 43.4% for K490 (see Table 9).

GLI CHLA ($CHLA_{GLI\_nLw}$) was scattered (underestimated) considerably from *in-situ* CHLA ($CHLA_{insitu}$) in the high-CHLA range (Fig. 6(a)). CHLA derived using *in-situ* nLws by the GLI in-water algorithm ($CHLA_{insitu\_nLw}$) was generally in agreement with $CHLA_{insitu}$ (Fig. 6(c)). However, $CHLA_{GLI\_nLw}$ was lower than $CHLA_{insitu\_nLw}$ in the high-CHLA range (Fig. 6(b)). The results indicate that the underestimation of $CHLA_{GLI\_nLw}$ in the high-CHLA range is caused by an error in the atmospheric correction, not the in-water algorithm.

Accuracies of SS and CDOM are important for the atmospheric correction algorithm because it uses SS and CDOM as inputs to an in-water optical model in the iteration process and absorptive aerosol correction (see Fig. 5). We should refine SS and CDOM retrievals further by
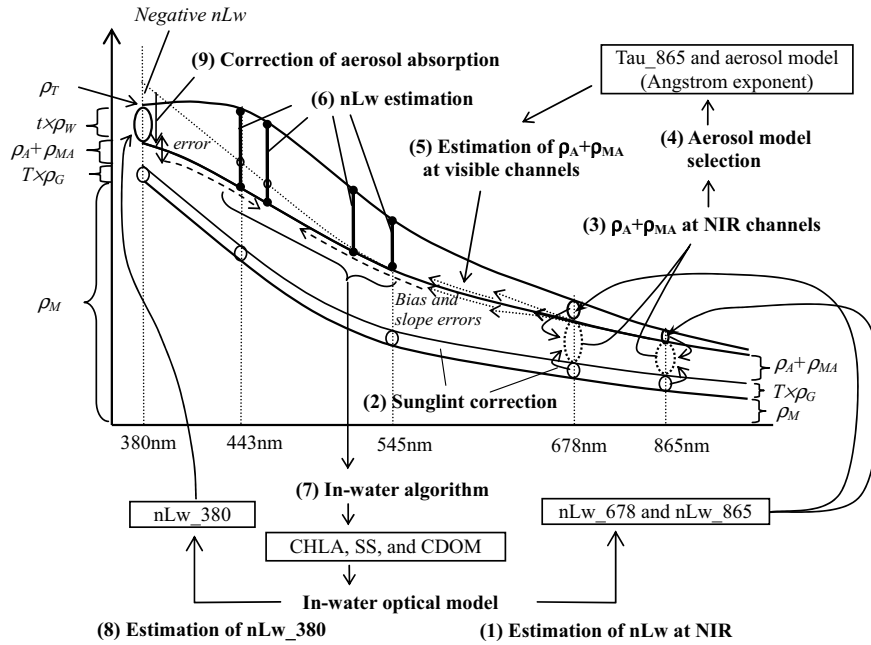
Fig. 5. GLI atmospheric correction scheme and error propagation.

making more *in-situ* measurements and improving the in-water optical model. For example, regional dependencies should be evaluated because the CDOM algorithm and the in-water optical model were developed based on *in-situ* observations in CalCOFI and near Japan areas, respectively (Kahru and Mitchell, 2001; Tanaka *et al.*, 2004).

GLI Tau_865 tended to be larger and Angstrom lower than *in-situ* values. GLI Tau_865 is in relatively better agreement with SIMBADA values than AERONET (Lanai) ones (SIMBADA: Yave/Xave = 1.19, N = 166; AERONET (Lanai): Yave/Xave = 3.72, N = 25). Similar errors have been reported in the aerosol products by SeaWiFS and MODIS (Fargion *et al.*, 2001; Fargion and McClain, 2003a). The possible causes of the bias are GLI calibration error in NIR channels, unexpected light from out of the GLI footprints, horizontal scattering light from land or cloud near the pixel, an error in estimate of sea-surface reflectance, etc., but the actual causes cannot be identified in this study.

5.2 Comparison with validation results from other sensors

The NASA Ocean Biology Processing Group has performed validations for SeaWiFS, OCTS, and Aqua MODIS. MedPDs were 33% and 17% for SeaWiFS CHLA and nLw_443, 46% and 25% for OCTS ones, and 41% and 21% for Aqua MODIS ones (McClain *et al.*, 2000; Fargion and McClain 2003b; Bailey and Werdell, 2005). In the match-up analysis, the samples were screened care-

fully using their quality flags and spatial uniformity tests (coefficient of variation of surrounding 3×3 pixel is less than 20%), which reduced the number of samples to about 38% of the no-overlapped original match-ups (McClain *et al.*, 2000). MedPD of GLI CHLA is a little larger (46.6% after QC) and the QC is looser (N is only reduced to 49%) than the values for SeaWiFS and MODIS. It is hard to use the same quality tests because flag sets and their thresholds are somewhat different according to the algorithm characteristics, e.g., cloud detection and absorptive aerosol correction. If we screened more samples using the flag set (c) in Table 7 similar to the SeaWiFS quality control, MedPD of CHLA was improved to 28.0%, but N decreased to 16 (6.8% of the original sample number). If we screened samples to a similar percentage to the SeaWiFS one (N = 81, 34% of the original sample number) by the flag set (b) in Table 7, MedPD of CHLA decreased to 42.4%. These results indicate that the GLI product accuracy is comparable to that of the SeaWiFS, OCTS and MODIS.

5.3 Discussion of error correlations

We investigated the reasons for the CHLA and nLw errors using correlations between parameters and their errors in Table 10.

(a) Aerosol estimation

Aerosol reflectances ($\rho_A + \rho_{MA}$) in visible channels are estimated based on Tau_865 and an aerosol model derived using NIR channels. The aerosol model describes the spectrum shape of the aerosol optical thickness and is
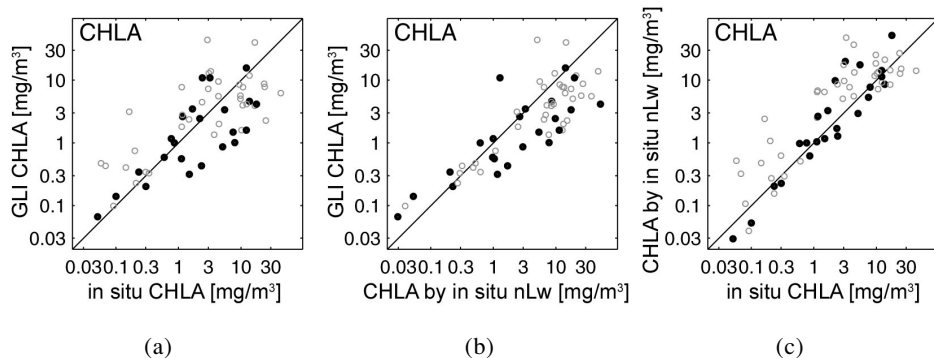
Fig. 6. Comparisons among *in-situ* CHLA, CHLA by *in-situ* nLw, and GLI CHLA using the common samples for all figures. Black points represent samples that passed QC; gray circle, samples screened by QC.

represented by the Angstrom exponent ((3)–(4)–(5) in Fig. 5). The estimation process causes strong correlations between nLw errors of different wavelengths. By using ratios between nLws in the empirical equations shown in Table 4, the influence of the aerosol estimation error is weakened in the CHLA estimate (this is the cause of no correlation between CHLA and nLw_565 in Table 10(a-3)).

Table 10(a-2) shows the nLw_443 was overestimated but not nLw_565 when Tau_865 was overestimated. The causes of the lack of correlation between Tau_865 and nLw_565 are possibly that influence of Angstrom and Tau_865 errors canceled each other because of the negative correlation between Tau_865 error and Angstrom error (Table 10(a-1)). On the other hand, the causes of the positive correlation between Tau_865 and nLw_443 are assumed to be that the influence of Angstrom error is stronger than the error of Tau_865 on nLw_443 because of the stronger influence of slope (Angstrom) than bias (Tau_865) far from the origin (678 and 865 nm) (see Fig. 5). The different responses in blue and green channels might cause negative correlation between Tau_865 and CHLA (we cannot confirm this because no CHLA observation was coincident with a Tau_865 observation in our samples).

(b) High in-situ nLw_680 condition

nLw_680, which is nearly zero in the clear water, is increased by in-water particle backscattering in the case of high CHLA or Case-2 waters. In such cases, estimates of nLws at NIR by an in-water optical model (Fig. 5(1)) can cause errors in aerosol estimates. Correlations in Table 10 (b) indicate that the algorithm treated a part of ρ_W as $\rho_A + \rho_{MA}$, and subtracted too much from ρ_T, causing a lower estimate of ρ_W in visible channels (cf. Figs. 5(1)–(3)–(4)–(5)–(6)). The situation can be viewed as an underestimation of nLws in visible channels. In contrast, there was no significant correlation between the nLw_680 error and the CHLA error because CHLA error is reduced

by using ratios between nLws, which have errors in the same direction.

(c) Absorptive aerosol correction

Absorptive aerosol correction incleases nLws at 380 nm to 520 nm according to the differences between nLw_380 derived by satellite and nLw_380 simulated by the in-water optical model using provisionally derived CHLA, SS, and CDOM during the iteration process (cf. Figs. 5(8)–(9)). The simulated nLw_380 can become too large where CHLA and CDOM are underestimated in the previous iteration. In this case, the absorptive correction works excessively, enhancing nLw in the blue channels and decreasing the CHLA and CDOM estimates (Figs. 5(9)–(6)–(7)). The underestimation of CHLA and CDOM causes the model's nLw_678 to be smaller and nLw_380 larger again (Figs. 5(1)–(3)–(4)–(6)). This feedback error sometimes occurs in the coastal areas due to too much in-water absorption by CDOM or mixture of CDOM and absorptive aerosol (e.g., "TKYOSGMI" cruise in Tokyo Bay).

(d) Sunglint

The correlation between Tau_865 error and sunglint reflectance (ρ_G) indicates that ρ_G is underestimated when sunglint is excessive. In this case, the algorithm subtracts the error of ρ_G as a part of aerosol ($\rho_A + \rho_{MA}$) in the estimation of nLws in visible channels. The cause of the correlation between ρ_G and nLw errors at 443 nm and 565 nm may be that the aerosol model selected by $\rho_A + \rho_{MA} +$ "ρ_G error" in the NIR band could not properly estimate the aerosol reflectance in the visible channels.

5.4 Items for the future

We have demonstrated that GLI ocean-color products achieved accuracies comparable with those of other current sensors, but better accuracy and spatial and temporal stability is still required for future applications including coastal monitoring and multi-sensor combined use. From this study, we have identified following items

that need to be improved in subsequent steps.

    a)   Improve the in-water optical model for estimating absorption and scattering from CHLA, SS, and CDOM in both offshore and coastal areas. For parameterization within the in-water optical model, we need to make *in-situ* databases for coastal areas. Consistent, accurate *in-situ* observations are important for this work. Protocols for *in-situ* measurements and processing should be improved and maintained to make the consistent datasets;

    b)   Improve absorptive aerosol correction, i.e., the characterization of spectrum of absorptive aerosols;

    c)   Address sea-surface reflection more precisely, including whitecaps and sunglint;.

    d)   Estimate the influence of horizontal scattering from neighboring bright targets (cloud and land); and

    e)   Improve shallow-water flagging with spectral transparency, depending on CHLA and SS.

Acknowledgements

References

Austin, R. W. (1974): The remote sensing of spectral radiance from below the ocean surface. p. 317–344. In *Optical Aspects of Oceanography*, ed. by N. G. Jerlov and E. S. Nielsen, Academic Press, London.

Bailey, S. and J. Werdell (2005): *Satellite-to-In Situ Match-up Results*. Available in http://seabass.gsfc.nasa.gov/matchup_results.html

Bécu, G., P.-Y. Deschamps and J.-M. Nicolas (2003): Validation of MERIS level-2 marine and aerosol products using SIMBADA radiometric in situ measurements. *MERIS and AATSR Validation Team Workshop*, ESRIN, Frascati, Italy, October 20–24, 2003.

Campbell, J. W. (1995): The Lognormal Distribution as a model for bio-optical variability in the sea. *J. Geophys. Res.*, **100**(C7), 13237–13254.

Clark, D. K., H. R. Gordon, K. K. Voss, Y. Ge. W. Brokenow and C. Trees (1997): Validation of atmospheric correction over oceans. *J. Geophys. Res.*, **102**, 17209–17217.

Cox, C. and W. Munk (1954): Measurements of the roughness of the sea surface from photographs of the sun's glitter. *J. Opt. Soc. Amer.*, **44**, 838–850.

Deschamps, P.-Y., B. Fougnie, R. Frouin, P. Lecomte and C. Verwaerde (2004): SIMBAD: a field radiometer for satellite ocean-color validation. *Applied Optics*, **43**(20), 4055–4069.

Dupouy, C., G. Dirberg, M. Tenorio, J. Neveux and A. L. Bouteiller (2004): Surveillance des Trichodesmium autour de la Nouvelle Calédonie, du Vanuatu, de Fidji et de Tonga (1998–2004). *Archives Sciences de la Mer, Océanographie*, Centre IRD de Nouméa, Nouvelle Calédonie, No. 7, 51 pp.

Esposito, J. A., X. Xiong, A. Wu, J. Sun and W. L. Barnes (2004): MODIS reflective solar bands uncertainty analysis. *Proc. SPIE Vol. 5542*, p. 448–458, Earth Observing Systems IX.

Fargion, G. S. and C. R. McClain (2003a): SIMBIOS Project 2002 Annual Report. *NASA Tech. Memo. 2003-211622*, NASA Goddard Space Flight Center, Greenbelt, MD, U.S.A., 157 pp.

Fargion, G. S. and C. R. McClain (2003b): MODIS Validation, Data Merger and Other Activities Accomplished by the SIMBIOS Project: 2002–2003. *NASA Tech. Memo. 2003-212249*, NASA/GSFC, Greenbelt, MD, U.S.A., 76 pp.

Fargion, G. S., R. Barnes and C. McClain (2001): In Situ Aerosol Optical Thickness Collected by the SIMBIOS Program (1997–2000): Protocols, and Data QC and Analysis. *NASA Tech. Memo. 2001-209982*, NASA Goddard Space Flight Center, Greenbelt, MD, U.S.A., 107 pp.

Fougnie, B., P.-Y. Deschamps and R. Frouin (1999): Vicarious Calibration of the POLDER ocean color spectral bands using *in-situ* measurements. *IEEE Trans. Geosci. Rem. Sen.*, **37**, 1567–1574.

Frouin, R. (2004): *GLI Algorithm Description (ATBD), Algorithm to Estimate Daily Photo-synthetically Available Radiation at the Ocean Surface*. Available in http://suzaku.eorc.jaxa.jp/GLI/ocean/algorithm/index.html

Frouin, R. and H. Murakami (2006): Estimating photosynthetically available radiation at the ocean surface from ADEOS-II global imager data. *J. Oceanogr*. (submitted).

Fukushima, H. (2004): *GLI Algorithm Description (ATBD), Atmospheric Correction for Ocean Color*. Available in http://suzaku.eorc.jaxa.jp/GLI/ocean/algorithm/index.html

Gordon, H. R. (1997): Atmospheric correction of ocean color imagery in the Earth Observation System era. *J. Geophys. Res.*, **102**(D14), 17081–17106.

Gordon, H. R. and A. Morel (1983): *Remote Assessment of Ocean Color for Interpretation of Satellite Visible Imagery*. Springer-Verlag, New York, 114 pp.

Ishizaka, J., K. Furuya, M. Kishino and K. Kawasaki (2001): Eisei kaishoku data kousei·kenshou no tame no kaiyo kansoku shishin, chikyu kagaku gijyutu forum/chikyu kansoku iinkai/kaiyo kankyo science team. ESTO 00P0A1-D010, 19 pp. (in Japanese).

Kahru, M. and B. G. Mitchell (1999): Empirical chlorophyll algorithm and preliminary SeaWiFS validation for the California Current. *Int. J. Remote Sensing*, **20**(17), 3423–3429.

Kahru, M. and B. G. Mitchell (2001): Seasonal and non-sea-

sonal variability of satellite-derived chlorophyll and CDOM concentration in the California Current. *J. Geophys. Res.*, **106**(C2), 2517–2529.

Kurihara, S., H. Murakami, K. Tanaka, T. Hashimoto, I. Asanuma and J. Inoue (2003): Calibration and instrument status of ADEOS-II Global Imager. *Proc. SPIE Vol. 5155.*

McClain, C. R., R. A. Barnes, R. E. Eplee, J. B. A. Franz, N. C. Hsu, F. S. Patt, C. M. Pietras, W. D. Robinson, B. D. Schieber, G. M. Schmidt, M. Wang, S. W. Bailey and P. J. Werdell (2000): SeaWiFS Postlaunch Calibration and Validation Analysis, Part 2. *NASA Tech. Memo. 2000-206892*, Vol. 10, ed. by S. B. Hooker and E. R. Firestone, NASA Goddard Space Flight Center, Greenbelt, MD, U.S.A., 57 pp.

Mitchell, B. G. and M. Kahru (1998): Algorithms for SeaWiFS standard products developed with the CalCOFI bio-optical data set. *Calif. Coop. Oceanic Fish. Invest. Rep.*, **39**, 133–147.

Mitchell, B. G. and M. Kishino (2004): *GLI Algorithm Description (ATBD) GLI In-Water Algorithms*. Available in http://suzaku.eorc.jaxa.jp/GLI/ocean/algorithm/index.html

Mitomi, Y., M. Toratani, M. Shimada, H. Oaku, H. Murakami, A. Mukaida, H. Fukushima and J. Ishizaka (1998): Evaluation of OCTS standard ocean color products: Comparison between satellite derived and ship measured values. p. 115–119. In *Proc. 4th PORSEC 1998*, Qingao, China, July 28–31, 1998.

Morel, A. and J.-F. Berthon (1989): Surface pigments, algal biomass profiles, and potential production of the euphotic layer: Relationships reinvestigated in view of remote-sensing applications. *Limnol. Oceanogr.*, **34**(8), 1545–1562.

Mueller, J. L., D. K. Clark, V. S. Kuwahara, G. Lazin, S. W. Brown, G. S. Fargion, M. A. Yarbrough, M. Feinholz, S. Flora, W. Broenkow, Y. S. Kim, B. C. Johnson, M. Yuen, P. G. Strutton, T. D. Dickey, M. R. Abbott, R. M. Letelier, M. R. Lewis, S. McLean, F. P. Chavez, A. Barnard, J. R. Morrison, A. Subramaniam, D. Manov, X. Zheng, L. W. Harding, Jr., R. A. Barnes and K. R. Lykke (2003): Ocean Optics Protocols For Satellite Ocean Color Sensor Validation, Revision 4, Volume V: Special Topics in Ocean Optics Protocols and Appendices. *NASA Tech. Memo. 2003-211621/Rev4-Vol. VI*, ed. by J. L. Mueller, G. S. Fargion and C. R. McClain, NASA Goddard Space Flight Center, Greenbelt, MD, U.S.A., 141 pp.

Murakami, H., M. Yoshida, K. Tanaka, H. Fukushima, M. Toratani, A. Tanaka and Y. Senga (2005): Vicarious calibration of ADEOS-2 GLI visible to shortwave infrared bands using global datasets. *IEEE Trans. Geosci. and Remote. Sens.*, **43**, No. 7, 1571–1584.

Nakajima, T. Y., T. Nakajima, M. Nakajima, H. Fukushima, M. Kuji, A. Uchiyama and M. Kishino (1998): Optimization of the Advanced Earth Observing Satellite II Global Imager Channels by use of Radiative Transfer Calculations. *Applied Optics*, **37**(15), 3149.

Neveux, J. and F. Lantoine (1993): Spectrofluorometric assays of chlorophylls and phaeopigments using the least-squares approximation techniques. *Deep-Sea Res. I*, **40**, 1747–1765.

O'Reilly, J. E., S. Maritorena, B. G. Mitchell, D. A. Siegel, K.

L. Carder, S. A. Garver, M. Kahru and C. McClain (1998): Ocean color chlorophyll algorithms for SeaWiFS. *J. Geophys. Res.*, **103**, 24937–24953.

Patt, F. S., R. A. Barnes, R. E. Eplee, Jr., B. A. Franz, W. D. Robinson, G. C. Feldman, S. W. Bailey, J. Gales, P. J. Werdell, M. Wang, R. Frouin, R. P. Stumpf, R. A. Arnone, R. W. Gould, Jr., P. M. Martinolich, V. Ransibrahmanakul, J. E. O'Reilly and J. A. Yoder (2003): Algorithm Updates for the Fourth SeaWiFS Data Reprocessing. *NASA Tech. Memo. 2003-206892*, Vol. 22, ed. by S. B. Hooker and E. R. Firestone, NASA Goddard Space Flight Center, Greenbelt, MD, U.S.A., 74 pp.

Shimada, M., H. Oaku, Y. Mitomi, H. Murakami, A. Mukaida, Y. Nakamura, J. Ishizaka, H. Kawamura, T. Tanaka, M. Kishino and H. Fukushima (1998): Calibration and validation of the ocean color version-3 product from ADEOS OCTS. *J. Oceanogr.*, **54**(5), 401–416.

Suzuki, R. and T. Ishimaru (1990): An improved method for the determination of phytoplankton chlorophyll using N,NDimethylformamide. *J. Oceanogr. Soc. Japan*, **46**, 190–194.

Tanaka, A., M. Kishino, R. Doerffer, H. Schiller, T. Oishi and T. Kubota (2004): Development of a neural network algorithm for retrieving concentrations of chlorophyll, suspended matter and yellow substance from radiance data of the ocean color and temperature scanner. *J. Oceanogr.*, **60**(3), 519–530.

Tanaka, A., H. Sasaki, Y. Toke, E. Siswanto, C. K. Tan, A. Wakamatsu and J. Ishizaka (2006): Developing an in-water algorithm for GLI using neural network technique with optical model based on optical properties in East China Sea, Ariake Sound and Isahaya Bay. *J. Oceanogr.* (submitted).

Tanaka, K., S. Kurihara and Y. Okamura (2005): The Sensor Characterization of Global Imager (GLI) on ADEOS-II Satellite, Vol. J88-B, No. 1, 151–157 (in Japanese).

Thuillier, G., M. Hers, P. C. Simon, D. Labs, H. Mandel, D. Gillotay and T. Foujols (2003): The solar spectral irradiance from 200 to 2400 nm as measured by the Solspec spectrometer from the Atlas and Eureca missions. *Solar Physics*, **214**(1), 1–22.

Toratani, M., H. Fukushima, H. Murakami and H. Kobayashi (2005): Atmospheric correction scheme for GLI in consideration of absorptive aerosol. *Proc. SPIE, Conf. Active and Passive Remote Sensing of the Oceans*, Vol. 5656, 45–53.

Toratani, M., H. Fukushima, H. Murakami and A. Tanaka (2006): Atmospheric correction scheme for GLI with absorptive aerosol correction. *J. Oceanogr.* (submitted).

Werdell, P. J. and S. W. Bailey (2005): An improved bio-optical data set for ocean color algorithm development and satellite data product validation. *Remote Sensing of Environment*, **98**(1), 122–140.

Xiong, X., K. Chiang, J. Esposito, B. Guenther and W. L. Barnes (2003): MODIS on-orbit calibration and characterization. *Metrologia*, **40** S89–S92.

Yoshida, M., H. Murakami, Y. Mitomi, M. Hori, K. J. Thome, D. K. Clark and H. Fukushima (2005): Vicarious calibration of GLI by ground observation data. *IEEE, Trans. Geosci. Remote Sens.*, **43**(10), 2167–2176.